Electronic and Chemical Properties of Nanostructured Cerium Dioxide Doped with Praseodymium

Holger Borchert,*,† Yulia V. Frolova,†,‡ Vasiliy V. Kaichev,† Igor P. Prosvirin,† Galina M. Alikina,† Anton I. Lukashevich,† Vladimir I. Zaikovskii,† Ella M. Moroz,† Sergei N. Trukhan,† Vyacheslav P. Ivanov,† Eugenii A. Paukshtis,† Valerii I. Bukhtiyarov,† and Vladislav A. Sadykov†,‡

Boreskov Institute of Catalysis SB RAS and Novosibirsk State University, Novosibirsk, Russia

Received: September 15, 2004; In Final Form: November 26, 2004

Nanostructured doped ceria is a prospective material for catalytic applications such as the construction of membranes with mixed electronic and ionic conductivity for effective syngas production. In this article, the surface properties of nanostructured ceria doped with praseodymium have been studied by X-ray photoelectron spectroscopy, secondary ion mass spectrometry, and Fourier transform infrared spectroscopy of adsorbed carbon monoxide. The effects of supporting 1.4 wt % Pt as well as structural changes upon the reduction of the samples with methane have been investigated. While in samples without supported platinum, mainly praseodymium cations are reduced in a methane atmosphere; stronger reduction of cerium cations was found in the case of surface modification with Pt. The structural differences correlate with results from temperature-programmed reaction experiments with methane. Explanations are discussed in terms of different reaction mechanisms.

1. Introduction

Ceria-based materials find a wide range of applications in the field of catalysis.[1−12] Some of the major examples are three-way catalysts,[5] selective oxidation or dehydrogenation of organic compounds,[6,7] solid oxide fuel cells,[8] and membranes for efficient methane conversion into syngas by the partial oxidation of methane.[9,10] In many of these applications, ceria is used as an oxygen storage material or as an oxygen ion conductor. Therefore, particular attention has been attracted by doped ceria. Doping with other rare-earth elements such as praseodymium or gadolinium creates oxygen vacancies which enable the migration of oxygen ions through the lattice and thus provide the materials with high oxygen ion conductivity.[11,12]

A new tendency in the past decade is the growing interest in the development and use of *nanostructured* ceria-based materials.[7,13−17] In a general manner, nanosized materials can present chemical and physical properties which differ from their bulk analogues. This gives rise to new possibilities to further modify the systems and to improve them with respect to technological applications.

Recently, we have reported on nanostructured Pr-doped ceria prepared by the so-called "Pechini method".[18,19] The system was found to have a high oxygen ion conductivity with the lattice oxygen mobility depending on the Pr content. Furthermore, as revealed by temperature-programmed reduction experiments, the promotion by platinum allows one to modify the reactivity of the lattice oxygen in the interaction with hydrogen and methane, which is technologically relevant for applications such as methane conversion into syngas.[18,19]

A better understanding of the influence of the amount of dopant ions, as well as the effect of surface modification with platinum on important characteristics such as the oxidation states of cerium and praseodymium ions or the reactivity with respect to the oxidation of methane, requires detailed analysis, in particular of the surface properties.

Therefore, the present article is devoted to surface science studies of the nanostructured ceria doped with praseodymium. Samples with and without promotion by platinum have been investigated by means of X-ray photoelectron spectroscopy (XPS) and Fourier transform infrared (FTIR) spectroscopy of adsorbed carbon monoxide. To have good reference data for the analysis of the doped systems, within the present work, we also recorded XPS spectra of pure oxides of cerium and praseodymium. In addition, the catalytically relevant redox properties of the doped cerium dioxide were studied by temperature-programmed reduction (TPR) techniques. Bulk structures of the samples were examined by powder X-ray diffraction (XRD) and transmission electron microscopy (TEM). Furthermore, secondary ion mass spectrometry (SIMS) was used to study the segregation behavior of the dopant ions at the surface.

2. Experimental Section

Dispersed samples of praseodymium-doped ceria were prepared by a polymerized complex precursor route known as the Pechini method[20] and calcined at 500 °C. Various samples are compared in the present work: pure cerium oxide, pure praseodymium oxide, doped cerium oxide samples with 10−50% Pr content, and a sample with 40% Pr content which additionally contains 1.4 wt % platinum supported by impregnation with water solutions of H_2PtCl_6.

The samples were studied by powder XRD, TEM, XPS, SIMS, FTIR spectroscopy of adsorbed CO probe molecules, and TPR in CH_4/He flow.

The XRD patterns were obtained using a URD-6 diffractometer with monochromated Cu Kα irradiation. A JEOL JEM-

* Corresponding author. E-mail: Holger_Borchert@gmx.net.
† Boreskov Institute of Catalysis SB RAS.
‡ Novosibirsk State University.

10.1021/jp045828c CCC: $30.25 © 2005 American Chemical Society
Published on Web 03/04/2005

2010 transmission electron microscope operating at 200 kV was used for TEM studies. Samples were prepared for the TEM measurements by ultrasonicating a small quantity of powder for a few minutes in ethanol. The resultant slurry was then deposited on a copper grid.

XPS experiments were performed with a VG ESCALAB HP spectrometer equipped with a hemispherical electron analyzer and an aluminum anode ($h\upsilon = 1486.6$ eV) operated at 200 W. All spectra were recorded with constant analyzer pass energy and a resolution of about 1.2 eV. Before the measurements, the spectrometer was calibrated using the Au $4f_{7/2}$ binding energy (BE) of 84.00 eV and the Cu $2p_{3/2}$ BE of 932.67 eV measured for clean gold and copper foils as references. The XPS analysis was performed at room temperature and pressures typically below 10^{-7} mbar. Because no carbon peak was observable, the constant energy shift caused by the charging effect (usually 5−10 eV) was corrected by referencing all the binding energies to the well-pronounced Ce $3d_{3/2}$ u‴ feature at 916.7 eV. In the case of the pure praseodymium oxide sample, no charging effect was observed. For each of the XPS spectra discussed in the following section, an attempt has been made to deconvolute the experimental curve into individual components, where the photoemission lines were simulated by Voigt line shapes. Quantitative analysis was performed from the integrated intensities of the XPS peaks corrected by the atomic sensitivity factors of the corresponding elements.[21]

Powder samples were pressed into a spoon-like copper sample-holder and have been investigated by XPS after two different treatments with oxygen and methane, respectively. The oxygen treatment was applied in situ (i.e., in the preparation chamber of the photoelectron spectrometer) where the samples were exposed for 1 h to 5000 Pa O_2 at 400 °C. Afterward, the samples were cooled to room temperature before the gas was pumped off and the sample transferred into the analyzer chamber where spectra were recorded in vacuo. (After removal of the gas, about 30 min passed before spectra could be recorded.) Methane treatments were partly performed ex situ. In a small, quartz glass reactor, the powder samples were subjected to a gas mixture of 50% CH_4/50% He at a flux rate of 4 L/h. The samples were heated to 750 °C and kept for 90 min at high temperature before cooling down to room temperature. The methane/helium flux was replaced by argon before the reactor was sealed. Samples were then transferred in the argon-filled sealed flasks to the photoelectron spectrometer and introduced into the preparation chamber under argon flow to minimize air contact. After this, the samples were in situ heated to the highest accessible temperature of about 540 °C and exposed to 5000 Pa CH_4 for 1 h. After the addition of methane, the temperature dropped to ∼490 °C after several minutes. Samples were finally cooled to room temperature before the gas was pumped off. It is noted here that XPS provided no evidence for carbon deposition on the samples after the exposure to methane at high temperature.

The sample preparation for SIMS included their rubbing into a high-purity indium substrate. An argon ion beam with energy of 3 keV and current density of 5 μA/cm^2 was used for the sputtering of the samples. A MC-7201 monopole mass spectrometer was used for the detection of the secondary ions. The signals at *m*/*e* values of 140 and 141 have been assigned to secondary ion currents of cerium and praseodymium ions, respectively. A possible small contribution of CeH species to the ion current with an *m*/*e* value of 141 has been neglected. The thickness of the layer etched out by argon bombardment was calculated from the sputtering time as described elsewhere.[22]

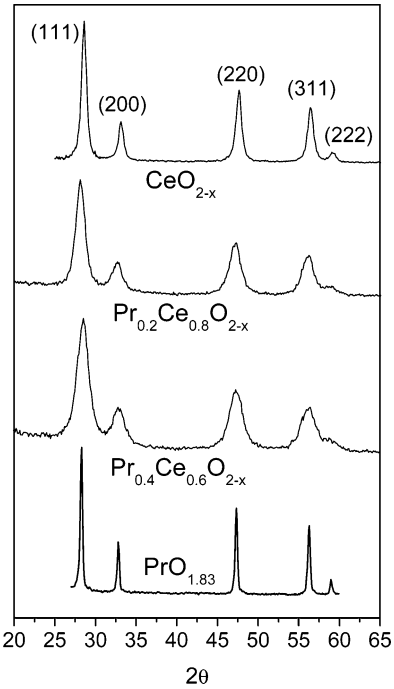

Figure 1. XRD patterns of the CeO_{2-x}, $Pr_{0.2}Ce_{0.8}O_{2-x}$, $Pr_{0.4}Ce_{0.6}O_{2-x}$, and $PrO_{1.83}$ samples.

FTIR spectra of adsorbed CO were obtained at 77 K using a Shimadzu FTIR-8300 spectrometer with a resolution of 4 cm^{-1}. Powder samples were pressed into self-supported wafers (20−30 mg/cm^2), which were pretreated in a vacuum during 90 min at 500 °C in situ in a specially designed IR cell. The CO adsorption was performed by the introduction of small doses of CO.

TPR experiments were carried out in a specially designed flow reactor. In a first step, 0.3 g of a given sample was pretreated for 40 min at 450 °C in a gas mixture of 1% oxygen in helium at a flux rate of 10 L/h. The sample was then cooled to room temperature in the oxygen/helium mixture. After this pretreatment, TPR was performed with a gas mixture of 1% methane in helium at a flux rate of 10 L/h. The temperature was linearly increased at a rate of 5 °C/min. Samples were finally kept for 70 min at the highest temperature of 880 °C. The gas mixture was analyzed with an IR absorbance gas analyzer. Results for the main reaction products CO and CO_2 are expressed in terms of consumed oxygen provided from the doped cerium oxide samples.

3. Results and Discussion

3.1. Structural Features. The known structure of cerium dioxide, as well as praseodymium dioxide, is the cubic fluorite type. Because the ionic radius of Pr^{4+} is very close to that of Ce^{4+} (0.96 and 0.97 Å, respectively), cerium and praseodymium oxide easily form solid solutions.[18,23−25] Indeed, according to XRD data, all praseodymium-doped ceria samples are single-phased and possess a fluorite-like structure. Typical XRD patterns are shown in Figure 1. The lattice parameter systematically increases with the dopant content (see Table 1), which provides evidence for the successful incorporation of dopant ions into the host lattice. The variation of the lattice parameter with the Pr content obtained in this work is in good agreement with those found for this system prepared via the hydrothermal route and calcined at 250 °C.[26] However, for samples of the Ce−Pr−O system sintered under air at 1400°C and containing only Pr^{4+} cations, the lattice parameter monotonically declines

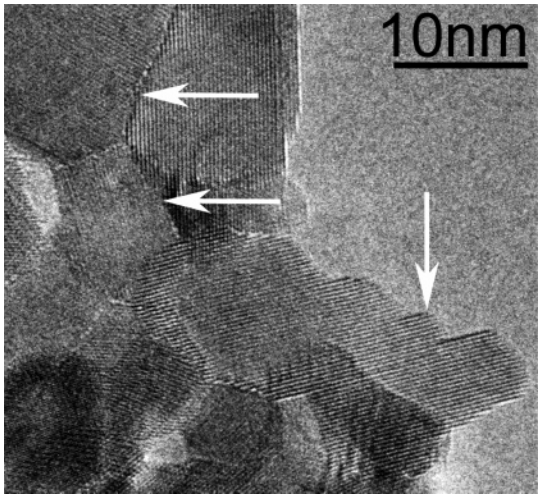

Figure 2. High-resolution transmission electron micrograph of the undoped cerium dioxide sample. Clearly resolved lattice fringes indicate a high degree of crystallinity within the domains of the nanostructured oxide. Intergrain boundaries and surface steps are observable and marked by arrows.

TABLE 1: Lattice Parameters and Domain Sizes as Determined by the Scherrer Equation for the Undoped and Doped Nanostructured Oxide Materials

sample	grain size [nm]	lattice parameter a [Å]
CeO_{2-x}	17.0	5.411
$PrO_{1.83}$	46.0	5.464
$Pr_{0.1}Ce_{0.9}O_{2-x}$	8.0	5.419
$Pr_{0.2}Ce_{0.8}O_{2-x}$	6.5	5.425
$Pr_{0.3}Ce_{0.7}O_{2-x}$	8.0	5.430
$Pr_{0.4}Ce_{0.6}O_{2-x}$	4.5	5.437
$Pr_{0.5}Ce_{0.5}O_{2-x}$	4.0	5.442

with increasing Pr content.[27] This suggests that, for samples prepared via low-temperature routes, the increase of the lattice parameter with increasing Pr content is due to the presence of Pr^{3+} ions.[18] Concerning the pure praseodymium oxide sample, it has to be mentioned that the XRD data matches the diffraction patterns of $PrO_{1.83}$ (ICDD file 06-0329) and Pr_6O_{11} (ICDD file 42−1121) better than that of PrO_2, which indicates a significant degree of oxygen deficiency.

A high-resolution TEM image of the pure cerium oxide sample is presented in Figure 2 and directly shows the nanostructured nature of the samples: nanocrystalline domains sintered to a dense body which presents a large number of probably disordered grain boundaries. The clearly visible lattice fringes give proof of a high degree of crystallinity within the domains. On the faces of the crystallites can be observed some small steps.

The nanostructured Pr-doped ceria samples present high specific surface areas of 50−100 m^2/g. A systematic decline of the specific surface area with increasing praseodymium content indicates a higher density of domain boundaries per unit surface at higher Pr content.[18]

The average sizes of the nanocrystalline domains were obtained from the width of the (311) reflection by means of the Scherrer equation[28]

$$d = \frac{K \cdot \lambda}{w \cdot \cos\theta} \tag{1}$$

where d is the domain size, λ is the wavelength of the irradiation, θ is the angle of the considered Bragg reflection, w is the width on a 2θ scale, and K is a constant close to unity which depends on factors such as the shape of the diffracting domains, and so on.[29,30] Because the TEM results do not provide clear evidence for a specific shape, K has been set to unity to give an estimate of the sizes of the nanocrystalline domains. We selected the (311) reflection for analysis, because at elevated Bragg angles, experimental errors are expected to be slightly smaller. Results are listed in Table 1. XRD particle sizes estimated using the Scherrer equation agree quite well with the TEM data and reveal a decline of the average domain size with increasing Pr content. This suggests that Pr tends to segregate at the grain boundaries, which prevents further growth of the domains.[18]

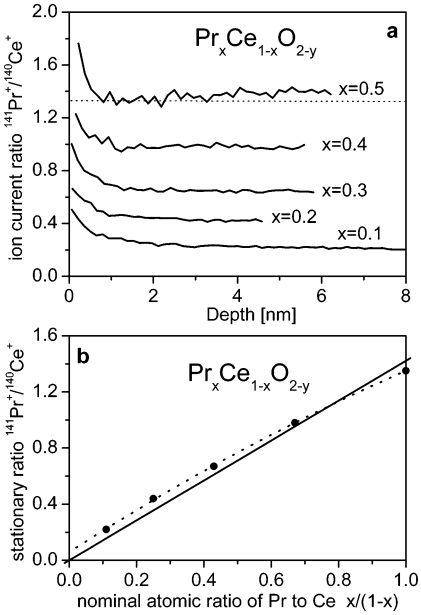

Figure 3. Part (a) shows secondary ion current ratios reflecting the segregation of praseodymium at the surface of the doped cerium oxide samples. In part (b), the nearly constant ratios found after removal of ∼1 nm of substance from the surface are plotted against the nominal atomic ratio of Pr to Ce. The experimental data (dots) are plotted together with a linear fit and a parabolic fit (solid and dotted lines).

The segregation behavior of the dopant ions in the host lattice has been studied by SIMS. Figure 3a shows the ratio of the secondary ion currents corresponding to Pr and Ce ions for samples with 10% to 50% praseodymium content as a function of depth. An enhanced ion current ratio at the beginning of the sputtering experiment reveals the segregation of praseodymium ions at the surface for all samples. After the removal of ∼1 nm of substance, the ion current ratio reaches a more or less constant level in all cases, which indicates a rather homogeneous distribution of the dopant ions in the volume of the nanocrystalline domains. For the sample with 50% praseodymium content, a very slight increase of the ion current ratio is observed after the removal of ∼4 nm of substance. This length corresponds to the domain size revealed by XRD, which is smaller at high doping rates (see Table 1). This result suggests that the segregation of praseodymium occurs not only at the surface but also at the grain boundaries between the nanocrystalline domains. A sharp peak can, however, not be observed by SIMS because of a too-broad distribution of domain sizes.

In Figure 3b, the value of the ion current ratio in the stationary regime (i.e., after removal of ∼1 nm of material) has been plotted against the nominal atomic ratio of Pr to Ce. Almost linear behavior is found. The very slight curvature indicates that the segregation of dopant ions is slightly more pronounced with increasing praseodymium content. The question of whether there is a preference for Pr^{3+} or Pr^{4+} ions to segregate at the surface cannot be fully answered here. One might expect the larger Pr^{3+}

ions to segregate preferentially,[31] but the systematic increase of the lattice parameter with increasing the doping rate shows that Pr^{3+} also is incorporated into the volume of the nanocrystalline domains.[18]

The segregation of praseodymium ions at the surface has also been studied by XPS. The total areas of the Pr 3d and Ce 3d peaks have been measured and divided by the corresponding atomic sensitivity factors which have been taken from the literature.[21] After the oxidation treatment, it was found that the calculated ratio exceeded the theoretical ratio for the case of homogeneous distribution of the dopant ions in the host lattice by ~20% and ~35% for the samples without and with supported Pt, respectively.[18] After reduction with methane, the excess of these ratios was enhanced to ~60% and ~50%, respectively. The observed increase is significantly higher for the samples without platinum, and as will be shown in section 3.2.3, in Pt-free samples, praseodymium is more strongly reduced upon treatment with methane. Thus, the results suggest that praseodymium ions which are initially in the +4 state tend to segregate to the surface when they are reduced to Pr^{3+}.

Samples have also been sputtered with argon in the preparation chamber of the photoelectron spectrometer. The analysis of Ce 3d and Pr 3d spectra after sputtering (not shown here) revealed large amounts of Me^{3+} cations (up to 50% for Ce^{3+} and 65% for Pr^{3+}) which suggests that the surface is oxygen-deficient after sputtering. This is a reasonable result, because oxygen is expected to be removed more easily by argon sputtering than the heavy metal cations. However, calculated atomic ratios of Pr to Ce showed no significant changes after these sputtering experiments. Here, it is important to note that SIMS is simply more surface-sensitive than XPS. While in SIMS experiments the substance removed from the surface is directly detected, in XPS experiments, the resulting surface after sputtering is observed. With Al Kα, radiation the mean free path length for Ce 3d and Pr 3d photoelectrons is on the order of ~1 nm. Because of the broad distribution of domain sizes, after sputtering, metal ions located at the grain boundaries are always expected to contribute significantly to the observable photoemission peak intensities. The observation that the atomic ratios of Pr to Ce determined by XPS do not significantly change after sputtering therefore suggests that the segregation of Pr occurs not only at the surface but also at the large number of grain boundaries in the nanostructured oxides.

Segregation of dopant cations at the surface and domain boundaries of ceria samples is a well-known phenomenon.[32] For nanocrystalline Pr-doped ceria, segregation of both Pr^{3+} and Pr^{4+} cations at the domain boundaries can create pathways for fast chemical diffusion of oxygen.[33]

3.2. Electronic and Chemical Properties. *3.2.1. Cerium Dioxide.* The XPS Ce 3d spectra of cerium compounds are well-known to be complicated because of hybridization of the Ce 4f orbitals with ligand orbitals and fractional occupancy of the valence 4f orbitals.[34−43] The XPS spectrum of the $3d_{5/2}$ cerium level will therefore be composed of three structures in the case of CeO_2 and only two structures in the case of Ce_2O_3 or other Ce^{3+} compounds.[34] This means that the interpretation of the Ce 3d spectra of partially reduced cerium oxide implies the complete analysis of ten peaks altogether, if we take into account the spin−orbit coupling.[35] Those ten peaks are usually labeled $v_0 \cdots v'''$ and $u_0 \cdots u'''$ in the literature. According to Romeo et al.,[35] v, v″, and v‴ are attributed to Ce $3d_{5/2}$ photoemission lines of CeO_2; v and v″ are due to a mixture of $(5d\ 6s)^0\ 4f^2\ O\ 2p^4$ and $(5d\ 6s)^0\ 4f^1\ O\ 2p^5$ configurations, while v‴ is a pure $(5d\ 6s)^0\ 4f^0\ O\ 2p^6$ final state. The lines v_0 and v′ are due to a mixture of $(5d\ 6s)^0\ 4f^2\ O\ 2p^4$ and $(5d\ 6s)^0\ 4f^1\ O\ 2p^5$ configurations in Ce_2O_3. The origin of the u structures, due to the Ce $3d_{3/2}$ sublevel, can be explained in the same way.

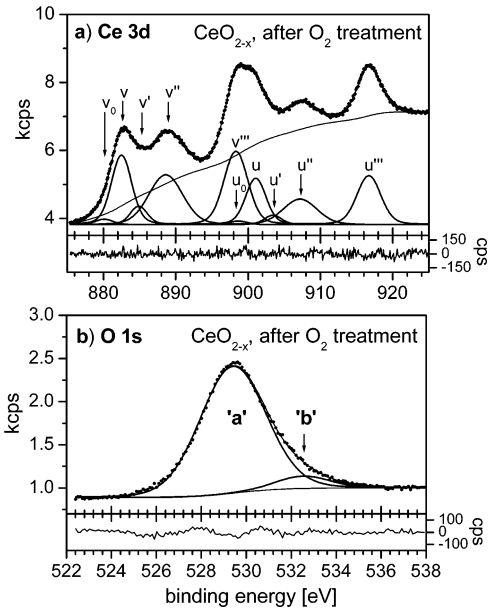

Figure 4. (a) The XPS Ce 3d spectrum of the nanostructured CeO_{2-x} sample. The experimental data (dots) are plotted together with a fit (solid lines). Deconvolution yields ten components labeled in analogy to common use in the literature.[35,43] A residual plot is given below the spectrum to judge the quality of the fit. (b) The XPS O 1s spectrum of the nanostructured CeO_{2-x} sample. Component "a" is attributed to O^{2-} ions. Component "b" can be assigned to $O^{\delta-}$ species or OH groups.

Figure 4a shows a Ce 3d spectrum of the nanocrystalline cerium oxide sample after in situ oxidation pretreatment. Deconvolution of the spectrum into its components yields five spin−orbit split doublets of Voigt functions. For fitting, a combined polynomial and Shirley-type background function was used. The Gaussian width was constrained to be identical for the two spin−orbit split peaks of a given doublet, but allowed to vary from one doublet to another. The Lorentzian width was constrained to be identical for all ten components and turned out to be 0.75 eV. The spin−orbit splitting was constrained to be identical for the doublets $v_0/u_0 \cdots v''/u''$ and found to be 18.57 eV. For the doublet v‴/u‴, a slightly reduced value of 18.39 eV had to be used. The branching ratio was fixed to the theoretical value of $^2/_3$ for the doublets v_0/u_0, v/u, and v‴/u‴. However, for the doublets v′/u′ and v″/u″, a reduced value of 0.51 was necessary to obtain a good fit. The binding energies of all ten peaks are summarized in Table 2 and are in good agreement with literature values which are also included in the table for comparison.[35,43]

The fitted intensity of the v and u features was used to calculate the relative amount of Ce^{3+}. While the peaks v, v″, v‴, u, u″, and u‴ are due to cerium ions in the +4 oxidation state, v_0, v′, u_0, and u′ reflect Ce^{3+} ions. One can determine the relative amount of cerium in the +3 oxidation state from the relative peak areas

$$\frac{[Ce^{3+}]}{[Ce^{3+} + Ce^{4+}]} = \frac{\text{area}(v_0, v', u_0, u')}{\text{total area}} \qquad (2)$$

where errors are estimated to be on the order of 5%.[38]

As to be expected for the sample discussed here, the cerium ions are almost exclusively in the +4 state after the applied oxidation procedure. Only about 8% of the ions were found to

TABLE 2: Binding Energies in eV for All Components of the Ce 3d Photoemission Spectra[a]

sample		v_0	v	v'	v''	v'''	u_0	u	u'	u''	u'''
ref 35		880.60	882.60	885.45	888.85	898.40	898.90	901.05	904.05	907.45	916.70
ref 43		880.1	882.3	884.8	888.8	898.2	898.8	901.0	903.5	907.4	916.7
CeO_{2-x}	O_2	880.1	882.5	884.9	888.6	898.3	898.7	901.1	903.4	907.2	916.7
$Pr_{0.2}Ce_{0.8}O_{2-x}$	O_2	880.2	882.5	884.6	888.8	898.3	898.7	901.1	903.2	907.4	916.7
	CH_4	880.4	882.6	884.9	888.6	898.3	899.0	901.2	903.5	907.2	916.7
$Pr_{0.4}Ce_{0.6}O_{2-x}$	O_2	880.7	882.6	884.8	888.8	898.3	899.3	901.2	903.4	907.4	916.7
	CH_4	880.5	882.6	884.7	888.8	898.3	899.0	901.1	903.2	907.3	916.7
$Pt/Pr_{0.4}Ce_{0.6}O_{2-x}$	O_2	880.9	882.4	884.3	888.8	898.3	899.4	901.0	902.9	907.4	916.7
	CH_4	880.3	882.5	884.4	888.8	898.2	898.9	901.1	903.0	907.4	916.7

[a] The values in the lines marked O_2 and CH_4 refer to results obtained after treatment of the samples with oxygen or methane, respectively.

TABLE 3: Atomic Fractions of the Ce and Pr Ions in the +3 Oxidation State after Treatment with Oxygen and Methane as Determined by Eqs 2 and 3

	$[Ce^{3+}]/[Ce^{3+}+Ce^{4+}]$ in %		$[Pr^{3+}]/[Pr^{3+}+Pr^{4+}]$ in %	
sample	after O_2	after CH_4	after O_2	after CH_4
CeO_{2-x}	8			
$PrO_{1.83}$			25	
$Pr_{0.2}Ce_{0.8}O_{2-x}$	6	10	51	63
$Pr_{0.4}Ce_{0.6}O_{2-x}$	7	8	52	65
$Pt/Pr_{0.4}Ce_{0.6}O_{2-x}$	7	35	33	39

be in the +3 state. Results for the oxidation states are summarized in Table 3.

It is necessary to note here that all calculations of this kind are performed assuming that the atomic ratio of 3+ ions to 4+ ions is spatially constant within the sample. Local variations of that atomic ratio due to segregation effects would affect the relative intensity of the corresponding peaks, because the attenuation of photoemission peaks depends on the length of the path which the photoelectrons have to travel through the sample. In the case of spatial variations of the atomic ratio of 3+ ions to 4+ ions, the real percentages may therefore systematically present slight deviations from the calculated numbers. Because concrete models for such spatial inhomogeneities are absent, calculations can only be performed for the approximation of a spatially constant atomic ratio of 3+ ions to 4+ ions here.

Figure 4b shows an O 1s spectrum fitted with two Voigt functions. The main component labeled "a" has a binding energy of 529.4 eV and is due to O^{2-} ions.[43] At the high-binding-energy side can be seen an additional peak labeled "b". In the presented fit, the binding energy is 532.5 eV, but the exact value is difficult to determine, because the peaks are rather broad and feature b is not very pronounced. The formation of $O^{\delta-}$ species or the presence of OH or CO_3 groups at the surface have been discussed as possible explanations for this component.[38,43] Evidence for the presence of OH groups at the surface is also provided by SIMS. An intensity ratio of about 0.15 was found for the ion currents corresponding to CeOH and Ce, respectively. Furthermore, OH groups have been found by FTIRS where bands at ~3640 cm^{-1} are observed. FTIRS also provides evidence for the presence of some carbonate groups (bands around 1380 and 1460 cm^{-1}), but no carbon peak was observed by XPS. Thus, carbonate groups are less likely here. Interestingly, the relative peak area of component b is about 7.4%, which is quite similar to the relative amount of Ce^{3+} ions. This is a remarkable result, because $O^{\delta-}$ species or OH groups are, in principle, expected to be located in the vicinity of Ce^{3+} ions. Thus, we suggest that the O 1s feature at 532.5 eV really corresponds to oxygen of a reduced ceria lattice.

3.2.2. Praseodymium Oxide. PrO_2 has a similar fluorite-like crystal structure, but it is black and conducting,[44] while CeO_2 is white and insulating. In comparison to cerium oxide, less literature is available on XPS of praseodymium oxide. Pr 3d spectra have a rather similar shape like the Ce 3d spectra of Ce(III)/Ce(IV) compounds and also allow us to study redox processes.[45] However, the precise analysis of the oxidation states by deconvolution of the spectra into components has been less elaborate until now.[23,36,46,47]

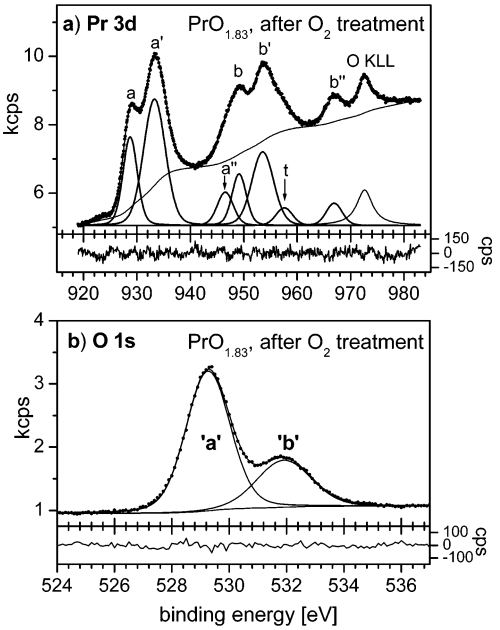

Figure 5. (a) The XPS Pr 3d spectrum of the nanostructured $PrO_{1.83}$ sample. Deconvolution yields three spin−orbit split doublets of Voigt functions labeled a/b, a′/b′, and a″/b″, as well as an extra feature labeled "t". On the high-binding-energy side, an oxygen Auger peak is also visible. (b) The XPS O 1s spectrum of the nanostructured $PrO_{1.83}$ sample. Component "a" is attributed to O^{2-} ions. Component "b" is assigned to $O^{\delta-}$ species or OH groups.

Figure 5a shows a Pr 3d spectrum of the nanocrystalline praseodymium oxide sample after the in situ oxidation treatment. The spectrum has been fitted using Voigt line profiles and a combined polynomial and Shirley-type background. Three spin−orbit split doublets labeled a/b, a′/b′, and a″/b″ were found. The $3d_{3/2}$ sublevel presents an additional feature labeled "t", which can be explained by a multiplet effect.[47] Furthermore, at the high-binding-energy side, a strong oxygen Auger peak is visible. The spectrum is basically similar to spectra reported in the literature.[23,46] Binding energies of the various components are summarized in Table 4. For fitting, the Lorentzian width was constrained to be identical for all components and found to be 0.62 eV. The Gaussian width was constrained to be identical for the two spin−orbit split peaks of a given doublet, but allowed to vary from one doublet to another. The spin−orbit splitting was constrained to be identical for doublets a/b and a″/b″ and turned out to be 20.40 eV. For doublet a′/b′, a slightly reduced value of 20.28 eV was found. The branching ratio was fixed to

TABLE 4: Binding Energies in eV for All Components of the Pr 3d Photoemission Spectra[a]

sample		*a*	*a′*	*a″*	*b*	*b′*	*b″*	*t*	% Pr^{3+}
$PrO_{1.83}$	O_2	928.7	933.3	946.5	949.1	953.6	966.9	957.6	25
$Pr_{0.2}Ce_{0.8}O_{2-x}$	O_2	928.6	933.1	946.3	949.1	953.7	966.8	957.6	51
	CH_4	928.7	933.0	945.8	949.3	953.5	966.4	957.7	63
$Pr_{0.4}Ce_{0.6}O_{2-x}$	O_2	928.6	933.2	946.0	949.0	953.6	966.5	957.3	52
	CH_4	928.7	933.1	945.7	949.1	953.5	966.1	957.1	65
$Pt/Pr_{0.4}Ce_{0.6}O_{2-x}$	O_2	928.9	933.3	946.4	949.3	953.7	966.8	957.6	33
	CH_4	928.9	933.2	946.1	949.5	953.6	966.7	956.7	39

[a] The values in the lines marked O_2 and CH_4 refer to results obtained after treatment of the samples with oxygen or methane, respectively.

$^2/_3$ for doublet a″/b″ and found to be 0.58 for doublets a/b and a′/b′. As already mentioned, Pr 3d spectra have been studied less extensively in the literature than Ce 3d spectra. There is no direct possibility reported to determine the amounts of praseodymium ions in the different oxidation states from the relative peak areas. Doublet a″/b″ is absent in the spectra of clean Pr_2O_3 and can therefore be assigned to Pr^{4+} ions.[47] However, doublets a/b and a′/b′ are present in Pr_2O_3 as well as in PrO_2 and cannot be assigned to a specific oxidation state. To estimate the amount of Pr^{3+} ions nevertheless, we proceeded as follows: Sinev et al.[23] published a fit of a Pr 3d spectrum which is very similar to our case. For a sample which was supposed to contain almost exclusively Pr^{4+} ions, a value of about 0.28 was obtained for the peak area ratio of a″/a′. Upon reduction of the sample, the area of peak a″ decreased while the area of a′ remained almost constant.[23] Thus, the peak area ratio of a″/a′ may be used to estimate the oxidation state of the praseodymium ions

$$\frac{[Pr^{3+}]}{[Pr^{3+} + Pr^{4+}]} = 1 - \frac{1}{0.28} \cdot \frac{\text{area}(a'')}{\text{area}(a')} \qquad (3)$$

Because the peak area ratio may, in principle, vary nonlinearly with the content of Pr^{3+} ions, the formula in eq 3 can only be considered as a rough approximation which is used here, because a more precise method is unfortunately absent at present. For the spectrum in Figure 5a, the formula yields 25% of praseodymium ions in the +3 oxidation state (see Table 3). This corresponds to a stoichiometric oxygen-to-praseodymium ratio of 1.875, in quite good agreement with the value of 1.83 (1.833) in $PrO_{1.83}$ (Pr_6O_{11}) as revealed by powder XRD. Indeed, oxygen-deficient nonstoichiometry of reducible Me^{4+} oxides such as CeO_{2-x} is accompanied by the presence of oxygen vacancies and Me^{3+} cations.[48]

The O 1s spectrum of the praseodymium oxide shows two well-resolved peaks (see Figure 5b). The main peak appears at 529.25 eV and is assigned to O^{2-} lattice ions. The peak labeled "b" is much better resolved than in the case of the cerium oxide sample. The feature b has a binding energy of 531.9 eV and can in analogy to the case of cerium oxide be assigned to the formation of $O^{\delta-}$ species or the presence of OH groups at the surface. The relative peak area is about 29%, which again is quite similar to the estimated percentage of Pr^{3+} ions.

In conclusion from the analysis of cerium and praseodymium oxide, correlation is found between the relative intensity of the high-binding-energy component in the O 1s spectra and the amount of metal ions in the +3 oxidation state. This is at least qualitatively in agreement with models where $O^{\delta-}$ species or OH groups should be located at Me^{3+} sites inside of the fluorite-like structure.

Quantitative interpretation of the results is rather difficult. Because of the stoichiometry of the oxides, one might, in principle, expect the percentages of $O^{\delta-}$ species/OH groups and Me^{3+} ions to present a ratio close to 1:2 instead of nearly 1:1.

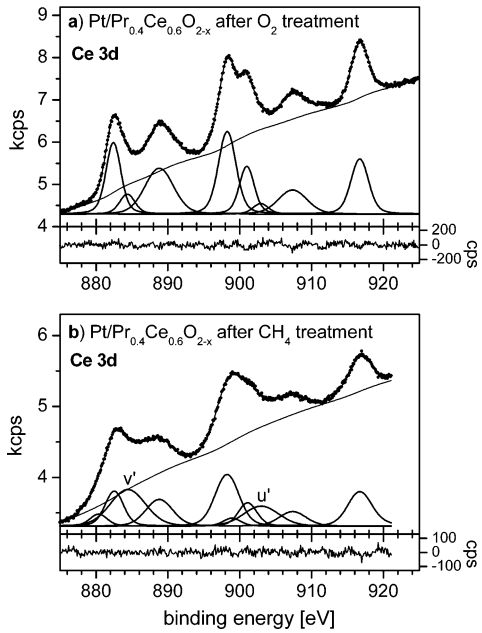

Figure 6. XPS Ce 3d spectra of the $Pt/Pr_{0.4}Ce_{0.6}O_{2-x}$ sample after oxygen (a) and methane (b) treatment. A strong increase in intensity of the doublet v′/u′ clearly indicates the reduction of cerium ions upon treatment with methane.

Because part of the Me^{3+} ions can be associated with oxygen vacancies in the lattice instead of $O^{\delta-}$ species/OH groups, the ratio should be even lower than 0.5. At least one reason the observed ratios are larger is simply related to the attenuation characteristics of photoemission peaks. The $O^{\delta-}$ species/OH groups are expected to be located mainly at the surface. By consequence, the relative intensity of the corresponding component in the O 1s spectra appears simply larger than that corresponding to O^{2-} ions, because the signal from the surface species is less attenuated.

3.2.3. Pr-Doped Cerium Oxide. Three Pr-doped cerium oxide samples have been studied by XPS: samples with 20% and 40% praseodymium content and a Pt-supported sample with 40% Pr content. The samples have been investigated after oxidation and after treatment with methane. Ce 3d spectra have been fitted in analogy to the spectrum of the pure cerium oxide sample shown in Figure 4a. The values of 0.75 eV for the Lorentzian width and 18.57 eV for the spin−orbit splitting of the doublets $v_0/u_0 \cdots v''/u''$ have been adopted from the former sample. All other constraints were applied similarly. The spin−orbit splitting of the doublet v‴/u‴ was found to be 18.43 ± 0.04 eV. The reduced value of the branching ratio for the doublets v′/u′ and v″/u″ was 0.55 ± 0.03.

Figure 6 shows Ce 3d spectra of the $Pt/Pr_{0.4}Ce_{0.6}O_{2-x}$ sample after oxygen (a) and methane (b) treatment. A strong increase of the doublet v′/u′ clearly shows the reduction of cerium ions upon the methane treatment. The relative amount of Ce^{3+} ions increases from ∼7% to ∼35% (see Table 3). For the samples

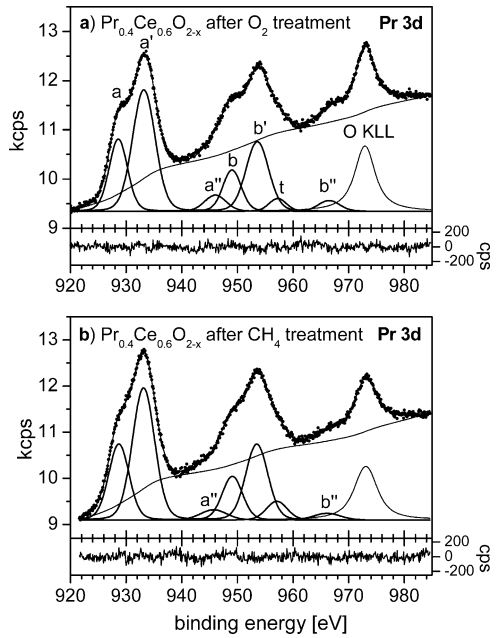

Figure 7. XPS Pr 3d spectra of the $Pr_{0.4}Ce_{0.6}O_{2-x}$ sample after oxygen (a) and methane (b) treatment. The decrease in intensity of doublet a″/b″ indicates the reduction of praseodymium ions upon treatment with methane.

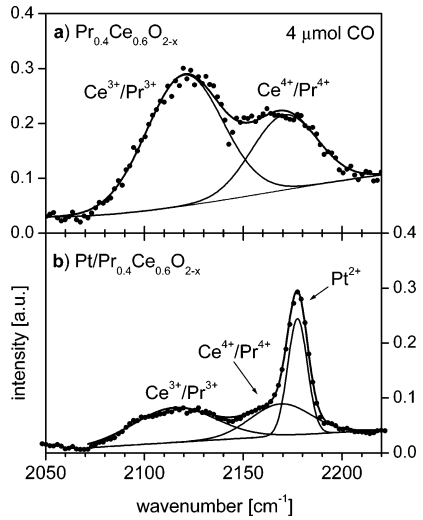

Figure 8. FTIR spectra of the $Pr_{0.4}Ce_{0.6}O_{2-x}$ (a) and $Pt/Pr_{0.4}Ce_{0.6}O_{2-x}$ (b) samples after exposure to 4 μmol (per pellet) carbon monoxide. Bands corresponding to Me^{3+} (Me = Ce, Pr), Me^{4+}, and Pt^{2+} ions are observed. In the Pt-supported sample, the intensity ratio of the bands corresponding to Me^{3+} and Me^{4+} ions, respectively, is reduced when compared to the sample without supported Pt.

without Pt, the relative amount of Ce^{3+} ions after the oxidation procedure is similar, but almost no increase is observed after reduction of the samples with methane.

It should be noted that we did not detect any effects of X-ray induced reduction of ceria. Recently, Paparazzo et al.[49,50] found that prolonged exposure of CeO_2 to X-rays causes the formation of some Ce^{3+} oxide species at the surface. In our experiments, we used comparable conditions, but the concentrations of Ce^{3+} species did not significantly change on the time scale of about 4−10 h, which was necessary to record all required XPS spectra for a given sample. This suggests that X-ray induced reduction of ceria is due to special types of defect sites or impurities which are absent in the nanostructured doped ceria samples.

Binding energies of the ten peaks of the Ce 3d level are summarized for the Pr-doped cerium oxide samples in Table 2. As the only irregularity, one can notice that the binding energy of doublet v′/u′ is about ∼0.4 eV lower for the Pt-supported sample. This suggests that platinum ions influence the electron density at surface Ce^{3+} sites.

Pr 3d spectra have been fitted in analogy to the spectrum of the pure praseodymium oxide sample presented in Figure 5a. The former value of 0.62 eV for the Lorentzian width has been adopted for analysis, all other constraints were applied similarly. The parameters showed no major variations. The spin−orbit splitting was found to be 20.5 ± 0.15 eV. The reduced value of the branching ratio for doublets a/b and a′/b′ was 0.57 ± 0.03. Figure 7 shows Pr 3d spectra of the sample $Pr_{0.4}Ce_{0.6}O_{2-x}$ after oxygen (a) and methane (b) treatment. One can see that the relative intensity of doublet a″/b″ corresponding to Pr^{4+} ions is reduced after reduction of the sample with methane. Calculation of the relative amounts of Pr in the different oxidation states yields an increase in the percentage of Pr ions in the +3 state from ∼50% to ∼65% (see Table 3). The loss of oxygen during treatment with methane is also reflected in a drop of the intensity of the oxygen Auger peak. For the sample with 20% Pr content, very similar results are found. The Pt-containing sample shows only about 33% of Pr^{3+} ions after the oxidation procedure and a less pronounced increase of this amount to ∼40% after reduction with methane. The strong influence of the surface modification with platinum on the oxidation states of praseodymium indicates that Pr^{3+} ions have a tendency to segregate to the surface. A theoretical study of the surface segregation phenomena in cerium dioxide by Sayle et al.[31] provides a possible reason for the reduced amount of Pr^{3+} ions in the case of surface modification with platinum: Defect clusters comprising oxygen vacancies and Pt^{2+} ions are supposed to be energetically favored when compared to clusters comprising oxygen vacancies and Me^{3+} ions.[31]

A lower amount of Me^{3+} ions in the case of supported platinum is also found by FTIRS of adsorbed CO. Figure 8 shows FTIR spectra of the samples with and without supported platinum at low CO coverage. For the sample without Pt, adsorption of CO gave rise to two broad peaks at 2120 and 2171 cm^{-1} (Figure 8a) which can be assigned to CO linearly adsorbed on coordinatively unsaturated Me^{3+} and Me^{4+} ions, respectively.[18,51,52] Figure 8b shows the corresponding spectrum for the sample with supported platinum. Absolute intensities are difficult to compare from one sample to another, but one can clearly see that the relative intensity of the band corresponding to Me^{3+} ions is significantly lower in the case of surface modification with Pt. Additionally, a band appears at 2178 cm^{-1} which can be assigned to the presence of Pt^{2+} ions at the surface.[18,52,53]

Comparing the Pt-free nanostructured samples to bulk Pr-doped ceria, we found our data to be in good agreement with a study by Sinev et al.[23] that states that Pr cations are more easily reduced than Ce cations. As an important difference, we note, however, that even after treatment in oxygen atmosphere, a relatively large amount of Pr ions were found to be in the +3 state for all studied samples. This should imply a large number of oxygen vacancies and high oxygen ion conductivity in the case of the nanostructured materials prepared by the Pechini method.

Binding energies of the Pr 3d photoemission peaks are summarized for the Pr-doped cerium oxide samples in Table 4. The binding energy of doublet a″/b″ seems to shift to slightly lower values with increasing Pr^{3+} content. Because doublet a″/b″ reflects Pr^{4+} ions, this suggests that an increasing degree of oxygen deficiency in the doped oxides also induces a slight

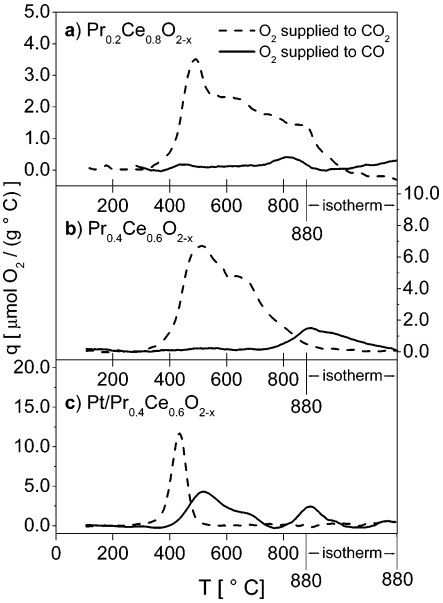

Figure 9. Results from TPR experiments with methane for Pr-doped samples without supported platinum (a, b) and with supported platinum (c). On the ordinate is plotted the amount of oxygen supplied from the samples, which after the reaction is present in form of CO_2 (dashed lines) and CO (solid lines). The data are normalized to 1 g of substance.

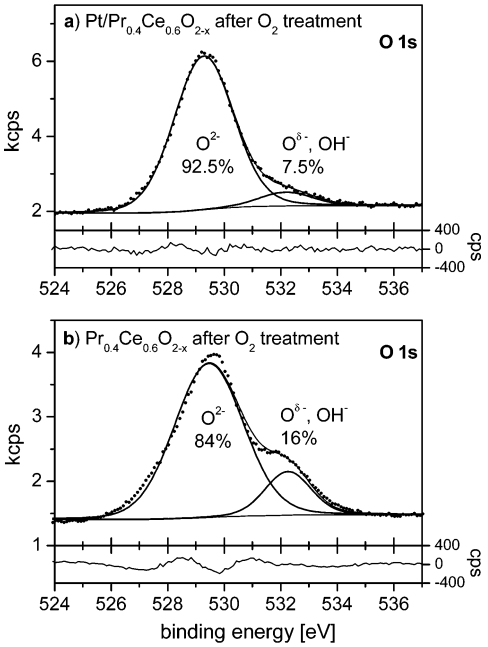

Figure 10. XPS O 1s spectra of the $Pt/Pr_{0.4}Ce_{0.6}O_{2-x}$ (a) and $Pr_{0.4}Ce_{0.6}O_{2-x}$ (b) samples after the oxidation treatment. The relative intensity of the peak corresponding to $O^{\delta-}$ species/OH groups is lower for the Pt-supported sample, which contains fewer Me^{3+} ions.

increase of the electron density at Pr^{4+} sites and therefore gives indications for induced structural disorder like the deformation of coordination polyhedra. An exact description of the induced defect structure cannot be given here.

In summary, there are almost no differences noticeable between the samples with 20% and 40% Pr content, but the Pt-supported sample interestingly shows a distinct behavior. Less Pr is found to be in the +3 state after the oxidation procedure, and methane seems to have a different effect. In the samples without supported Pt, mainly praseodymium ions are reduced, while cerium is almost not affected. In contrast, the Pt-supported sample shows a drastic increase of the amount of Ce^{3+} ions upon treatment with methane, while Pr is less affected.

This behavior correlates with differences observed in TPR experiments with methane. Figure 9 shows CH_4 TPR results for the three samples in question. The amount of oxygen supplied from the samples to the two reaction products carbon monoxide (desired reaction for syngas production) and carbon dioxide (concurrent reaction) is plotted against the temperature. The samples without supported platinum show quite similar behavior. At about 400 °C, the deep oxidation reaction of methane to CO_2 starts. The corresponding TPR maxima are observed at 490 and 510 °C for the samples with 20% and 40% Pr content, respectively. Considerable syngas production only starts at temperatures around 750 °C. The maxima for CO are observed at 820 and 880 °C, respectively. The TPR curves for the platinum-supported sample are different. Modification with Pt shifts the TPR peak corresponding to CO_2 to slightly lower temperatures. The maximum is observed at 435 °C. The main difference is a large shift of the TPR peak corresponding to CO to lower temperatures. Already at temperatures around 500 °C, syngas production is the dominant reaction here.

Thus, the correlation between the differences in the CH_4 TPR experiments and the different reduction behavior of cerium and praseodymium ions revealed by XPS suggests that the concurring reactions of methane conversion into CO_2 or CO take place via different mechanisms involving the reduction of mainly praseodymium or cerium cations, respectively.

XPS O 1s spectra of the Pr-doped cerium oxide samples with and without supported Pt are presented in Figure 10. Again, two peaks are observed at binding energies of 529.4 and 532.2 eV. The component corresponding to $O^{\delta-}$ species/OH groups is more pronounced in the case of the Pt-free sample which contains more Me^{3+} ions. This is in good agreement with the observations discussed already for the undoped oxides.

Because surface modification with platinum dramatically affects the catalytic properties,[18,19] the analysis of platinum sites in the doped system is of special interest. Pt 4f spectra of the supported sample are presented in Figure 11. The spectrum recorded after the oxidation procedure (Figure 11a) could not be fitted with satisfactory quality with only one doublet of the Voigt functions. On the other hand, unambiguous fitting with more than one doublet of the Voigt functions is difficult here, because the spectrum is too noisy because of the low Pt content of only 1.4 wt % in the sample. Therefore, we proceeded as follows: The spectrum after treatment with methane (Figure 11b) is fittable with acceptable quality with only one doublet using values of 0.3 eV for the Lorentzian width and 3.35 eV for the spin−orbit splitting. A binding energy of 71.6 eV was found for the Pt $4f_{7/2}$ peak. That value was adopted for fitting of the spectrum in Figure 11a (i.e., the binding energy of one doublet was fixed to 71.6 eV in the presented fit). The binding energy of the Pt $4f_{7/2}$ peak of the second doublet was then found to be 74.2 eV. Whereas the species with the higher binding energy can clearly be identified as Pt^{2+} ions,[54,55] the species at 71.6 eV requires discussion. Bulk metallic platinum has, in principle, a binding energy of ∼71.1 eV, but slightly higher values have already been reported for small platinum clusters with sizes below 2 nm.[54,56] Thus, the species at 71.6 eV might correspond to small metallic Pt clusters at the surface. Another possible interpretation for the observed peak is Pt^{+} species.

The second interpretation is favored by results from FTIRS of adsorbed CO, which at higher CO coverage provide evidence for the presence of Pt^{+} ions at the surface. Figure 12 shows spectra of the Pr-doped samples with and without supported Pt. The spectra differ from those in Figure 8, because the

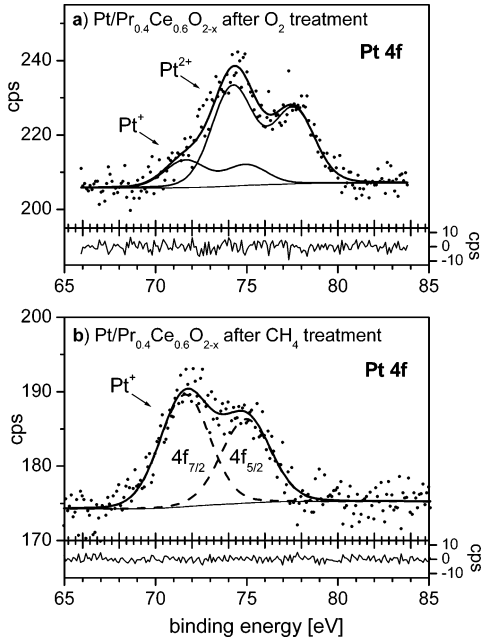

Figure 11. XPS Pt 4f spectra of the $Pt/Pr_{0.4}Ce_{0.6}O_{2-x}$ sample after oxygen (a) and methane (b) treatment. The solid lines represent spin−orbit split doublets of Voigt functions. The decomposition into two components corresponding to the Pt $4f_{7/2}$ and $4f_{5/2}$ sublevels is shown in part (b) (dashed lines). In the oxidized state, evidence for Pt^{2+} and Pt^{+} species is found. Upon treatment with methane, Pt^{2+} is entirely reduced to Pt^{+}.

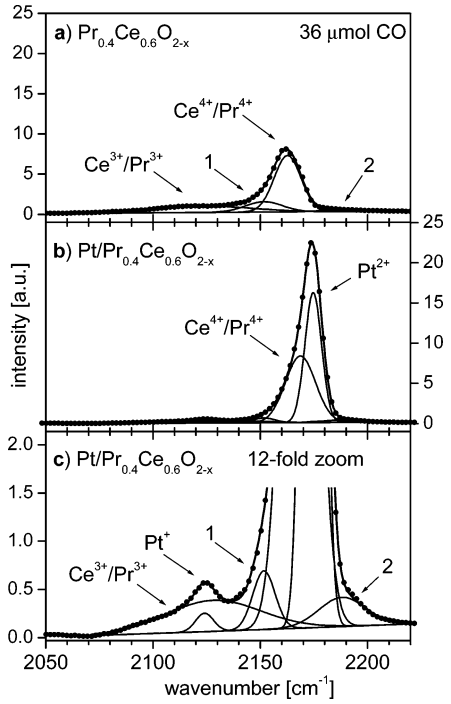

Figure 12. FTIR spectra of the $Pr_{0.4}Ce_{0.6}O_{2-x}$ (a) and $Pt/Pr_{0.4}Ce_{0.6}O_{2-x}$ (b, c) samples after exposure to 36 μmol of carbon monoxide (per pellet); (c) is a twelvefold zoom into (b) and provides evidence for Pt^{+} species.

adsorption of CO to available surface sites depends quite strongly on the CO pressure. For the sample without Pt (Figure 12a), the two ν(C−O) bands corresponding to CO linearly adsorbed on Me^{3+} and Me^{4+} ions are observed at 2123 and 2163 cm^{-1}. Additionally, two weak bands appeaer at around 2152 and 2188 cm^{-1} (labeled "1" and "2" in Figure 12), but their exact positions and relative intensities are difficult to determine, because these bands are weak and poorly resolved. By consequence, a clear interpretation of these two features is not possible here. Figure 12b,c shows the corresponding spectrum for the Pt-supported sample. Figure 12c is simply a zoom into Figure 12b. Again, one can notice a reduced Me^{3+}-to-Me^{4+} ratio. The week band at 2124 cm^{-1} can be assigned to Pt^{+} ions.[18,52] Metallic platinum should by reflected by a band around 2060 cm^{-1},[52] but is absent here. Thus, the photoemission peak observed at 71.6 eV is most likely due to Pt^{+} ions, and the results show reduction of Pt^{2+} to Pt^{+} upon treatment with methane.

3.3. Considerations on the Reaction Mechanism of Methane Conversion into Syngas. The mechanism of the reaction of methane conversion into syngas is a complicated topic of current research and depends on the reaction conditions and the system used as catalyst.[57−60] Although we can certainly not present a full description of the reaction mechanism in our case, a possible scenario may shortly be discussed here for the studied system of Pr-doped ceria. Otsuka et al. investigated the partial oxidation of methane to synthesis gas over cerium dioxide and proposed that the reaction involves the adsorption of methane on reduced surface sites (i.e., at clusters of Ce^{3+} ions and oxygen vacancies[60]). After cleavage of all four C−H bonds, oxygen shall be supplied from the lattice to the adsorbed carbon. Finally, CO is supposed to desorb from the surface, followed by recombination of the H atoms to H_2.[60] The recombination or desorption of hydrogen was supposed to be the rate-determining step for methane conversion into syngas. Because the presence of Pt remarkably decreased the desorption temperatures for H_2 and CO, it was suggested that Pt accelerated this step through a reverse spillover mechanism.[60]

If we extend this model, it might be possible that deep oxidation to CO_2 occurs if the CO molecule is not released from the surface quickly enough but oxidized further by another O^{2-} ion. This is likely to occur when methane is adsorbed to defect sites at the numerous grain boundaries where O^{2-} ions are expected to be easily released, which of course favors deep oxidation. This process seems to take place at moderate temperatures in the case of the Pt-free samples. Moreover, at moderate temperatures, the activation of methane on defect sites of fluorite-like oxides characterized by decreased oxygen-cation bond strength proceeds via the formation of oxygenates such as formates[61] and formaldehyde[62] as revealed by FTIRS. These rather strongly bound species are mainly transformed into deep oxidation products because of the interaction with the reactive oxygen forms supplied by diffusion along the grain boundaries. Because our investigations revealed significant segregation of Pr ions at the surface and at the grain boundaries (see section 3.1 and Figure 3), it is reasonable that the release of oxygen from defect sites at the grain boundaries is accompanied by the reduction of mainly Pr ions. Thus, one can understand why the deep oxidation of methane to carbon dioxide leads to the preferential reduction of Pr^{4+} to Pr^{3+} in the case of the Pt-free samples.

Surface modification with Pt, which appears to be distributed rather uniformly on the surface on both regular and defect sites, can enable another reaction pathway for the oxidation of methane. According to in situ FTIRS experiments, the reaction of methane conversion into syngas over Pt-modified Ce-based catalysts proceeds through a carbon intermediate.[60] Indeed, Pt is known to efficiently activate methane by the cleavage of C−H bonds.[63,64] The resulting CH_x fragments ($x = 0, 1, 2, 3$) are expected to be quickly released from the Pt ions/atoms and to adsorb to nearby surface sites.[65] Because, even for the nano-

structured doped ceria, the grain boundaries cover only a small fraction of the entire surface, adsorption of the CH_x fragments occurs with higher probability to regular surface sites. Subsequent migration to defect sites at the grain boundaries is unlikely, because activated methane (carbon or CH_x fragments) was reported to have only a low mobility on the cerium oxide surface.[64]

On the regular surface sites, on-top oxygen forms are characterized by heats of adsorption up to 60−80 kcal/mol, which is higher than the heat of oxygen adsorption at defect sites (∼ 40 kcal/mol).[66] Thus, the reactivity of regular surface oxygen is reduced when compared to oxygen at defect sites at the grain boundaries. This favors the partial oxidation of adsorbed CH_x fragments to CO and H_2. The reaction is expected to occur by interaction of the CH_x fragments with the on-top oxygen forms on the regular centers, which are then replenished by diffusion of O^{2-} ions from the lattice. Because of the stoichiometry of the mixed oxides and the segregation of Pr at the surface, the lattice is somewhat depleted by Pr. Therefore, the diffusion of the lattice oxygen to the surface results in the reduction of mainly Ce^{4+} ions located within the probing depth of XPS. This provides a possible explanation for the partial oxidation of methane to carbon monoxide observed as the dominant reaction at moderate temperatures in the case of surface modification with Pt and may be why this reaction is accompanied by the reduction of mainly Ce cations.

A final proof for the different reaction mechanisms in the two cases can certainly not be given by our investigations, but all results strongly point toward a situation like in the scenario described in the preceding paragraph.

4. Summary

Nanostructured cerium dioxide samples doped with praseodymium have been compared in terms of their surface properties. The oxidation states of cerium and praseodymium ions have been determined by XPS. While cerium is mainly in the +4 oxidation state, about one-half of the praseodymium ions were found to be in the +3 state. The large amount of Pr^{3+} cations seems to be a particularity of the *nanostructured* doped ceria samples prepared by the Pechini method.

Segregation of the praseodymium ions at the surface and probably also at the numerous grain boundaries is observed by XPS and SIMS. There are some indications that the larger Pr^{3+} ions tend to preferentially segregate, but analysis of the lattice parameters determined by XRD shows that Pr^{3+} is at least partially also incorporated into the volume of the nanocrystalline domains. Additionally, a doped sample with 1.4 wt % supported platinum was investigated. Only about 33% of the Pr ions were found to be in the +3 state, and the segregation effect was slightly more pronounced.

Upon reduction of the samples with methane, a different behavior was observed for the samples with and without supported platinum. While in the Pt-free samples, mainly praseodymium cations were reduced in methane atmosphere, the strong reduction of cerium cations was found in the case of surface modification with platinum. This result correlates with substantially different observations in TPR experiments with methane. Without supported platinum, the main reaction at temperatures up to about 750 °C is the deep oxidation of methane and its conversion into CO_2. In the case of supported Pt, already at temperatures above ∼500 °C, the partial oxidation of methane dominates (i.e., the desired reaction for syngas production). The XPS results therefore suggest that the two concurring reactions take place via different mechanisms which imply the reduction of mainly praseodymium or cerium, respectively. Possible reaction mechanisms have briefly been discussed. In conclusion, the present analysis contributes to the detailed elucidation of the structural, electronic, and chemical properties of doped nanostructured ceria and points out correlations of the electronic properties with important characteristics for catalytic applications.

Acknowledgment. This work was partially supported by the INTAS 01-2162 and ISTC 2529 Projects, Integration Project 39 of SB RAS, and Project #3N-292-03 of the Ministry of Russian Education. Furthermore, H.B. is grateful for support by a fellowship within the Postdoc program of the German Academic Exchange Service (DAAD).

References and Notes

(1) Trovarelli, A., Ed. *Catalysis by Ceria and Related Materials*; Imperial College Press: London, 2002.
(2) Trovarelli, A.; Leitenburg, C.; Boaro, M.; Dolcetti, G. *Catal. Today* **1999**, *50*, 353.
(3) Valenzuela, R. X.; Bueno, G.; Corberan, V. C.; Xu, Y.; Chen, Ch. *Catal. Today* **2000**, *61*, 43.
(4) Montoya, J. A.; Romero-Pascual, E.; Gimon, C.; Del Angel, P.; Monzon, A. *Catal. Today* **2000**, *63*, 71.
(5) He, H.; Dai, H. X.; Ng, L. H.; Wong, K. W.; Au, C. T. *J. Catal.* **2002**, *206*, 1.
(6) Yao, C.-S.; Weng, H.-S. *Ind. Eng. Chem. Res.* **1998**, *37*, 2647.
(7) Concepcion, P.; Corma, A.; Silvestre-Albero, J.; Franco, V.; Chane-Ching, J. *J. Am. Chem. Soc.* **2004**, *126*, 5523.
(8) Haile, S. M. *Mater. Today* **2003**, *6*, 24.
(9) Sammells, A. F.; Schwartz, M.; Mackay, R. A.; Barton, T. F.; Peterson, D. R. *Catal. Today* **2000**, *56*, 325.
(10) Ishihara, T.; Takita, Y. *Catal. Surv. Jpn.* **2000**, *4*, 125.
(11) Kharton, V. V.; Yaremchenko, A. A.; Naumovich, E. N.; Marques, F. M. B. *J. Solid State Electrochem.* **2000**, *4*, 243.
(12) Skinner, S.; Kilner, J. A. *Mater. Today* **2003**, *6*, 30.
(13) Tschöpe, A.; Ying, J. Y.; Tuller, H. L. *Sens. Actuators, B* **1996**, *31*, 111.
(14) Chiang, Y.-M.; Lavik, E. B.; Kosacki, I.; Tuller, H. L.; Ying, J. Y. *J. Electroceram.* **1997**, *1*, 7.
(15) Valenzuela, R. X.; Bueno, G.; Solbes, A.; Martinez, E.; Cortez Corberan, V. *Top. Catal.* **2001**, *15*, 181.
(16) Wang, Z. L.; Feng, X. *J. Phys. Chem. B* **2003**, *107*, 13563.
(17) Deshpande, A. S.; Pinna, N.; Beato, P.; Antonietti, M.; Niederberger, M. *Chem. Mater.* **2004**, *16*, 2599.
(18) Sadykov, V. A.; Frolova, Yu. V.; Alikina, G. M.; Lukashevich, A. I.; Muzykantov, V. S.; Rogov, V. A.; Moroz, E. M.; Zyuzin, D. A.; Ivanov, V. P.; Trukhan, S. N.; Zaikovskii, V. I.; Borchert, H.; Paukshtis, E. A.; Bukhtiyarov, V. I.; Kaichev, V. V.; Prosvirin, I. P.; Neophytides, S.; Kemnitz, E.; Scheurell, K. *React. Kinet. Catal. Lett.*, in press.
(19) Sadykov, V. A.; Frolova, Yu. V.; Alikina, G. M.; Lukashevich, A. I.; Neophytides, S. *React. Kinet. Catal. Lett.*, in press.
(20) Pechini, M. P. Method of preparing lead and alkaline earth titanates and niobates and coating method using the same to form a capacitor. U.S. Patent 3,330,697, July 11, 1967.
(21) Wagner, C. D., Riggs, W. M., Davis, L. E., Moulder, J. F., Muilenberg, G. E., Eds. *Handbook of X-ray Photoelectron Spectroscopy*; Perkin-Elmer Corporation: Eden Prairie, MN, 1979.
(22) Ilinitsch, O. M.; Nosova, L. V.; Gorodetskii, V. V.; Ivanov, V. P.; Trukhan, S. N.; Gribov, E. N.; Bogdanov, S. V.; Cuperus, F. P. *J. Mol. Catal. A: Chem.* **2000**, *158*, 237.
(23) Sinev, M. Yu.; Graham, G. W.; Haack, L. P.; Shelef, M. *J. Mater. Res.* **1996**, *11*, 1960.
(24) Logan, A. D.; Shelef, M. *J. Mater. Res.* **1994**, *9*, 468.
(25) McBride, J. R.; Hass, K. C.; Poindexter, B. D.; Weber, W. H. *J. Appl. Phys.* **1994**, *76*, 2435.
(26) Greenblatt, M.; Shuk, P.; Huang, W.; Dikmen S.; Croft, M. *Mater. Res. Soc. Symp. Proc.* **1999**, *548*, 511.
(27) Takasu, Y.; Sugino, T.; Matsuda, Y. *J. Appl. Electrochem.* **1984**, *14*, 79.
(28) Klug, H. P.; Alexander, L. E. *X-ray Diffraction Procedures for Polycrystalline and Amorphous Materials*, 2nd ed.; John Wiley & Sons: New York, 1974.
(29) Langford, J. I.; Wilson, A. J. C. *J. Appl. Crystallogr.* **1978**, *11*, 102.
(30) Natter, H.; Schmelzer, M.; Löffler, M.-S.; Krill, C. E.; Fitch, A.; Hempelmann, R. *J. Phys. Chem. B* **2000**, *104*, 2467.

(31) Sayle, T. X. T.; Parker, S. C.; Catlow, C. R. A. *J. Phys. Chem.* **1994**, *98*, 8, 13625.
(32) Ito, Y.; Lei, Y.; Browning, N. D.; Mazanec, T. J. *Mater. Res. Soc. Symp. Proc*. **2002**, *703*, 489.
(33) Knauth, P.; Tuller, H. L. *Mater. Res. Soc. Symp. Proc*. **1999**, *548*, 429.
(34) Park, P. W.; Ledford, J. S. *Langmuir* **1996**, *12*, 1794.
(35) Romeo, M.; Bak, K.; El Fallah, J.; Le Normand, F.; Hilaire, L. *Surf. Interface Anal.* **1993**, *20*, 508.
(36) Burroughs, P.; Hammett, A.; Orchard, A. F.; Thornton, G. *J. Chem. Soc., Dalton Trans*. **1976**, *17*, 1686.
(37) Wuilloud, E.; Delley, B.; Schneider, W.-D.; Baer, Y. *Phys. Rev. Lett.* **1984**, *53*, 202.
(38) Laachir, A.; Perrichon, V.; Badri, A.; Lamotte, J.; Catherine, E.; Lavalley, J. C.; El Fallah, J.; Hilaire, L.; Le Normand, F.; Quemere, E.; Sauvion, G. N.; Touret, O. *J. Chem. Soc., Faraday Trans*. **1991**, *87*, 1601.
(39) Herman, G. S.; Kim, Y. J.; Chambers, S. A.; Peden, C. H. F. *Langmuir* **1999**, *15*, 3993.
(40) Shyu, J. Z.; Weber, W. H.; Gandhi, H. S. *J. Phys. Chem*. **1988**, *92*, 4964.
(41) Thormat, N.; Gautier-Soyer, M.; Bordier, G. *Surf. Sci*. **1996**, *345*, 290.
(42) Liu, G.; Rodriguez, J. A.; Hrbek, J.; Dvorak, J.; Peden, C. H. F. *J. Phys. Chem. B* **2001**, *105*, 7762.
(43) Hardacre, C.; Roe, G. M.; Lambert, R. M. *Surf. Sci.* **1995**, *326*, 1.
(44) McKelvy, M.; Eyring, L. R. *J. Cryst. Growth* **1983**, *62*, 635.
(45) Lütkehoff, S.; Neumann, M.; Slebarski, A. *Phys. Rev. B* **1995**, *52*, 13808.
(46) Bianconi, A.; Kotani, A.; Okada, K.; Giorgi, R.; Gargano, A.; Marcelli, A.; Miyahara, T. *Phys. Rev. B* **1988**, *38*, 3433.
(47) Ogasawara, H.; Kotani, A.; Potze, R.; Sawatzky, G. A.; Thole, B. T. *Phys. Rev. B* **1991**, *44*, 5465.
(48) Creaser, D. A.; Harrison, P. G.; Morris, M. A.; Wolfindale, B. A. *Catal. Lett*. **1994**, *23*, 13.
(49) Paparazzo, E. *Surf. Sci*. **1990**, *234*, L253.
(50) Paparazzo, E.; Ingo, G. M.; Zacchetti, N. *J. Vac. Sci. Technol., A* **1991**, *9*, 1416.
(51) Bozon-Verduraz, F.; Bensalem, A. *J. Chem. Soc., Faraday Trans*. **1994**, *90*, 653.
(52) Hadjiivanov, K. I.; Vayssilov, G. N. *Adv. Catal.* **2002**, *47*, 307.
(53) Jin, T.; Zhou, Y.; Mains, G. J.; White, J. M. *J. Phys. Chem.* **1987**, *91*, 5931.
(54) Fleisch, T. H.; Mains, G. J. *J. Phys. Chem.* **1986**, *90*, 5317.
(55) Drawdy, J. E.; Hoflund, G. B.; Gardner, S. D.; Yngvadottir, E.; Schryer, D. R. *Surf. Interface Anal*. **1990**, *16*, 369.
(56) Cheung, T. T. P. *Surf. Sci*. **1984**, *140*, 151.
(57) Hu, Y. H.; Ruckenstein, E. *J. Phys. Chem. B* **1998**, *102*, 230.
(58) Wang, H. Y.; Ruckenstein, E. *J. Phys. Chem. B* **1999**, *103*, 11327.
(59) Freni, S.; Calogeor, G.; Cavallaro, S. *J. Power Sources* **2000**, *87*, 28.
(60) Otsuka, K.; Wang, Y.; Sunada, E.; Yamanaka, I. *J. Catal.* **1998**, *175*, 152.
(61) Odier, E.; Schuurman, Y.; Barral, K.; Mirodatos, C. *Stud. Surf. Sci. Catal.* **2004**, *147*, 79.
(62) Zhu, J.; van Ommen, J. G.; Lefferts, L. *J. Catal.* **2004**, *225*, 388.
(63) Aghalayam, P.; Park, Y. K.; Fernandes, N.; Papavassiliou, V.; Mhadeshwar, A. B.; Vlachos, D. G. *J. Catal.* **2003**, *213*, 23.
(64) Fathi, M.; Bjorgum, E.; Viig, T.; Rokstad, O. A. *Catal. Today* **2000**, *63*, 489.
(65) Martins, R. L.; Baldanza, M. A.; Souza, M. V. M.; Schmal, M. *Stud. Surf. Sci. Catal.* **2004**, *147*, 643.
(66) Bulgakov, N. N.; Sadykov, V. A.; Lunin, V. V.; Kemnitz, E. *React. Kinet. Catal. Lett.* **2002**, *76*, 111.